Journal of Materials Chemistry C

ROYAL SOCIETY OF CHEMISTRY

PAPER

View Article Online
View Journal | View Issue



Cite this: J. Mater. Chem. C, 2024, 12, 13353

# Boosting solar cell performance during highly thermo- and photo-stable asymmetric perylene diimide dimeric acceptors by selenium-annulation at the outside bay position†

Junfeng Tong, ‡*[a] Jiayu Fang,‡[a] Lili An,[b] Youzhi Huo,[c] Fushui Di,[a] Pengzhi Guo,[a] Chunyan Yang,[a] Zezhou Liang,[d] Jianfeng Li[a] and Yangjun Xia*[a]

Asymmetric perylene diimide (PDI)-based dimeric electron acceptors have received relatively little attention. Herein, two asymmetric fused PDI dimers, namely **PDI-TPDI** and **PDI-SePDI**, linked through one single bond (σ bond), were synthesized by S/Se-annulation at the outside bay position. Both of them exhibited outstanding thermal-stability with a 5% decomposition temperature of higher than 400 °C and good photostability. After replacing S-annulation with Se-annulation, a blue-shifted absorption peak, weakened aggregation, deepened $E_{LUMO}$, but almost unchanged molecular twisting angle between two aromatic rings were observed. Accordingly, the Se-annulated **PDI-SePDI**-based device achieved a 56.64% elevated PCE as high as 5.31% with a slightly decreased $V_{OC}$ of 0.70 V, a 55.91% increased $J_{SC}$ of 14.64 mA cm$^{-2}$, a 3.45% enhanced FF of 51.84%, and the S-annulated **PDI-TPDI**-based device obtained the PCE of 3.39%. The PCE enhancement was mainly due to the enhanced exciton dissociation, suppressed charge recombination, and increased charge mobility, benefiting from the beneficial microstructural morphology as the result of larger heteroatom Se-annulation. This work revealed the regulating mechanism of Se-annulation of PDI at the outside position on molecular distortion, morphology and photovoltaic performance.

Received 14th May 2024,
Accepted 14th July 2024

DOI: 10.1039/d4tc01986e

rsc.li/materials-c



## Introduction

Recently, non-fullerene electron acceptors (NFEAs) have received increasing attention due to unparalleled advantages including synthetic flexibility, no batch-to-batch difference, broad and strong absorption ranging from ultraviolet-visible (UV-vis) to near-infrared (NIR) area, tuneable energy levels, improved morphological stability, and small driving force to guarantee efficient exciton dissociation.[1–7] Furthermore, the power conversion efficiencies (PCEs) of NFEAs-based organic solar cells (OSCs) have increased sharply[8–10] and surpassed those of fullerene-based OSCs.[11] Commonly, solution processed NFEAs were classified into two categories on the basis of chemical structure, including the fused aromatic ITIC derivatives featuring the acceptor–donor–acceptor (A–D–A) framework[12,13] and/or ladder type Y series acceptors[14] and rylene imide derivatives, especially perylene diimide (PDI) derivatives with an A–DA′D–A structure.[15–18] Although the development of PDI-based acceptors has lagged behind that of A–D–A type acceptors, they are considered to be very promising building blocks for constructing efficient photovoltaic (PV) semiconductors, owing to their attractive characteristics including the excellent light-absorbing (400–600 nm) and electron-withdrawing ability, outstanding thermal- and photo-robustness, high electron mobility up to $10^{-4}$–$10^{-3}$ cm$^2$ V$^{-1}$ s$^{-1}$, and facile chemical modifications at multiple positions.[1,6,19–25]

Apart from the above merits, PDI derivatives with low synthetic complexity and cheap production costs also possess excellent photochemical stability and have been widely applied in car paint, which remains stable for many years under the

[a] Gansu Provincial Engineering Research Center for Organic Semiconductor Materials and Application Technology, School of Materials Science and Engineering, Lanzhou Jiaotong University, Lanzhou 730070, China. E-mail: tongjunfeng139@163.com, xiayangjun2015@126.com
[b] School of Chemical Engineering, Northwest Minzu University, Lanzhou 730030, China
[c] Harbin Station, China Railway Harbin Group Co., Ltd, Harbin 150010, China
[d] Key Laboratory for Physical Electronics and Devices of the Ministry of Education & Shaanxi Key Lab of Information Photonic Technique, School of Electronics and Information Engineering, Xi'an Jiaotong University, Xi'an 710049, China

† Electronic supplementary information (ESI) available. See DOI: https://doi.org/10.1039/d4tc01986e

‡ These authors contributed to this work equally.

conditions of sunlight.[1,26] Despite these advantages, the anisotropic characteristics made PDI molecules tend to form microscale or sub-microscale aggregates along the direction of a planar perylene backbone, resulting in an oversized phase separation in the bulk-heterojunction (BHJ) blend film.[27–29] Additionally, the large aggregation would precipitate the formation of an excimer, leading to an irreversible loss of photo-induced excitons, which trapped excitons by shortening the diffusion length.[30] Although charge mobility can be enhanced to a certain degree, owing to the 5–20 nm excitation diffusion length, it will undoubtedly impede the excitation diffusion. Additionally, it will reduce the exciton dissociation because of the slashed D/A interfaces and eventually hurt the device performance. For overcoming this issue and alleviating the strong aggregation, several productive strategies have been put forward and many efficient twisted PDI acceptors have been designed. Constructing a PDI-based monomer PDFC with an A–DA′D–A motif,[31] dimers SF-PDI$_2$[15] and SF-iPDI2[32] with a spirofluorene (SF) linker and SdiPBI-Se with a single bond linker,[16] trimers Ta-PDI with an electron-deficient 1,3,5-triazine (Ta) linker[1] and TPO-PDI with a triphenylphosphine monoxide (TPO) linker,[17] tetramers FTTB-PDI4 with a tetrathienylbenzene (TTB) linker[18] and SF-iPDI4[32] and SF-PDI4[33] with an SF linker and BPT-Se1 with an *i*-BDT-Th linker,[3] multimer CRP-1 with a corannurylene pentapetalae (CRP) linker[34] *etc.* achieved a balance between high exciton dissociation and efficient charge transfer and thereby acquired an inspirational PV performance with a PCE ranging from 5.31% to 12.56%. Early in 2014, the dovetail shape side chain-containing PDI dimer (s-diPBI) with a single linker exhibited the 3.63% PCE, which was significantly higher than those (1.54% and 1.36%) of (d-diPBI) with double linkage and (t-diPBI) with triple linkage when paired with PBDTTT-C-T.[35] Meanwhile, Jen *et al.* extended the dovetail side chain from heptane-4-yl to undecane-6-yl and obtained di-PBI, the PCE of the PBDTT-F-TT:di-PBI-based device was significantly increased to 5.90% after optimization by the inverted device and the modified zinc oxide interlayer.[36] Afterwards, they continued to change the linking modes and developed two dimers H-di-PDI and B-di-PDI, with the torsion angle between two PDI subunits of 70° for bay-linking B-di-PDI and 90° for imide-linking H-di-PDI. Hence, the **PTB7-Th**:H-di-PDI-based device afforded a higher PCE of 6.41% due to the high-efficient exciton dissociation and charge percolation pathways as the result of better miscibility, predominate face-on orientation and suitable aggregation domains.[37] In 2017, three PDI diploids with a shorter pentan-3-yl side chain, namely, *bb*-2PDI (*bay*-/*bay*-), *oo*-2PDI (*ortho*-/*ortho*-) and *bo*-2PDI (*bay*-/*ortho*-), connected at different linking positions were developed *via* the Ullmann coupling reaction, with the dihedral angles of 70°, 87° and 67°, respectively. Dimer *oo*-2PDI exhibited the highest $E_{LUMO}$ of −3.90 eV, resulting in the relatively higher open-circuit voltage ($V_{OC}$) of 0.799 V, and favourable morphology, relatively higher and balanced charge mobility made **PTB7-Th**:*oo*-2PDI-based device afford the excellent short-circuit current density ($J_{SC}$) up to 18.79 mA cm$^{-2}$ and markedly outperformed PCE of 8.30%.[38] Apparently, constructing PDI dimers with appropriate twisted architecture and fewer synthesis steps was an effective method for exploring high-performance NFEAs.

Recently, heteroatom annulation was demonstrated to be one effective and feasible strategy for fine-tuning the molecular structure and electronic density due to van der Waals and heteroatom–heteroatom interaction.[16,39–41] In 2015, Wang *et al.* modulated the molecule *via* the S-annulation strategy and obtained the dimer SdiPBI-S with a dihedral angle of 80°, a higher absorption coefficient ($\varepsilon$) up to 1.4 × 10$^5$ M$^{-1}$ cm$^{-1}$ at 504 nm, and an elevated $E_{LUMO}$ of −3.85 eV. Thus, an excellent PCE of 7.16% was found when blending with PDBT-T1, exhibiting a high $V_{OC}$ of 0.90 V, a $J_{SC}$ of 11.98 mA cm$^{-2}$, and an FF of 66.1% after applying 0.75% DIO additive.[39] As an alternative to the sulfur atom, the more easily polarized selenium atom possesses a larger and looser outermost electron cloud, effectively enhancing the orbital overlap and improving the charge transfer capability. Inspired by this, the Se-annulation analogue SdiPBI-Se, exhibiting the slightly reduced dihedral angle of 77°, the comparable $\varepsilon$ of 1.04 × 10$^5$ M$^{-1}$ cm$^{-1}$, and the slightly down-shifted $E_{LUMO}$ of −3.87 eV, was developed. The better photon absorption, charge transfer and ultrafast charge generation promoted the PDBT-T1:SdiPBI-Se-based device to deliver the synergistically increased $V_{OC}$ of 0.96 V, $J_{SC}$ of 12.49 mA cm$^{-2}$, and FF of 70.2% and thus elevated the PCE up to 8.4%.[16] In 2020, Zhou *et al.* chose the planar vinylene as a central linker and synthesized a series of fused PDI dimers, V-TDI$_2$ and V-FDI$_2$ fused with thiophene and furan at the inside-bay position and V-PDIS$_2$ and V-PDISe$_2$ fused with the S atom and the Se atom with a larger radius at the outside-bay position, utilizing fusion-free V-PDI$_2$ as the reference. It was exhibited that V-TDI$_2$ and V-FDI$_2$ afforded a planar molecular structure and raised the $E_{LUMO}$, giving a higher $V_{OC}$ of 0.97 and 1.00 V, while V-PDIS$_2$ and V-PDISe$_2$ adopted the twisted molecular configuration with a dihedral angle of 81–82°, delivering the larger $J_{SC}$ of 9.41, 10.00 mA cm$^{-2}$ and a lower $E_{LUMO}$. Accordingly, the external-annulation PBDB-T:V-PDIS$_2$- and PBDB-T:V-PDISe$_2$-based devices got the winning PCE of 5.76% and 6.51%.[40] Meanwhile, Bo *et al.* synthesized the two Se-annulation PDI acceptors VDP-Se and NDP-Se at the outside-bay position and found that VDP-Se had a slightly twisted configuration (11.7°), while NDP-Se exhibited a distorted naphthalene core and X-shaped skeleton with a dihedral angle of 34.9°. Two planar PDI arms not only guaranteed enough solubility but also suppressed the oversized aggregation. Finally, the PBDB-T:NDP-Se-based device yielded the 23.29% increased PCE of 7.41%.[41] It should be noted that constructing the asymmetric molecules was also a powerful method for developing efficient PV materials due to the higher dipole moment and larger intermolecular binding energy than their symmetric counterparts.[42,43] In 2018, the asymmetric linker 6-(thien-2-yl)-benzo[*b*]thiophene (T-BTh) and the two dimers unfused A101 and fused A102 were developed. The increased effective π-conjugation and decreased torsion angle produced a favourable morphology and enhanced π–π stacking, resulting in better charge mobility. Thus, a 57.82% increased PCE of

 

5.65% was achieved in the PBDB-T:A102-based device.[44] Meanwhile, Zhang *et al.* developed two Se-annulation PDI dimers FPDI-Se with one selenophene heterocycle and FPDI-2Se with two selenophene heterocycles and found that the facilitated molecular stacking and intermolecular charge transport made the asymmetric **PTB7-Th**:FPDI-Se-based device obtain the 48.54% elevated PCE of 6.61%.[45] Assisted by Se-annulation and fused by a thiophene at the outside-bay position, three asymmetric fused dual-PDI acceptors with the dovetail shape tridecane-7-yl side chain, termed as PDI2-Se fused with the Se atom, PDI2-FT fused with the thiophene ring and PDI2Se-FT both fused with Se atom and thiophene were developed by Xia's group, exhibiting the X-shaped configuration with similar dihedral angles of 24.2°–25.2° and close $E_{LUMO}$ of −3.76 to −3.71 eV. PDI2Se-FT afforded the highest PCE of 6.96% when paired with PBDB-T.[46] However, the correlation between the molecular structure and PV performance during these heteroatom annulation PDI dimers is still unclear. It is not definite that the twisted molecular structure was most favourable for enhancing the device performance. Accordingly, it was of significant importance and highly urgent to explore the new asymmetric PDI dimers and further elaborate the interplay of structure–property–performance.

In consideration of the abovementioned merits of S/Se-annulation and the advantages of asymmetric PDI acceptors, herein, two asymmetric S/Se-annulation PDI dimeric electron acceptors, named **PDI-TPDI** and **PDI-SePDI** (Chart 1), were synthesized *via* the tetrakis(triphenylphosphine)platinum(0)-catalyzed Suzuki coupling reaction. The influence of the different annulation types on the molecular twisting configuration, thermo-/photo-stability, absorption, energy level, molecular stacking and aggregation, charge transfer, miscibility and morphology of the blend film together with the PV performance were systematically investigated. Both asymmetric acceptors possessed excellent thermo-/photo-stability and a similar dihedral angle between two PDI sub-planes of approximately 67°. Furthermore, replacing S-annulation with Se-annulation weakened the molecular aggregation, making the **PTB7-Th**:**PDI-SePDI**-based device achieve a PCE up to 5.31%.

## Results and discussion

### Synthesis and characterization

As elucidated in Scheme 1, the monobromides **TPDIBr** and **SePDIBr** were synthesized *via* two synthetic steps including S/Se-annulation and mono-bromination reactions. The starting material mononitrated PDI-HD-$NO_2$ was synthesized according to a reported method.[21] Annulation with S or Se powder in the solvent of *N*-methylpyrrolidone (NMP) at a high temperature of 190 °C produced the fused PDI moieties TPDI and SePDI with yields of 67% and 65%, respectively. Next, monobrominating TPDI and SePDI with liquid bromine ($Br_2$) utilizing ferric chloride ($FeCl_3$) as a catalyst gave rise to monobromide **TPDIBr** and **SePDIBr** in yields of 63% and 61%, respectively. Meanwhile, the PDI-HDBr reacted with bis(pinacolato)diboron, utilizing the Pd(dppf)$Cl_2$ as a catalyst in the presence of $K_2HPO_4$, forming the monoborate ester **PDI-Bpin** in a yield of 42%.[47] The targeted asymmetric S/Se-annulation PDI dimeric acceptors **PDI-TPDI** and **PDI-SePDI** were prepared *via* a classical Suzuki coupling reaction with yields of 25% and 23% (Table S1, ESI†), respectively.[48] Chemical structures of the S-annulation intermediates TPDI and Se-annulation one SePDI, mono-bromides **TPDIBr** and **SePDIBr**, monoboric ester **PDI-Bpin**, and targeted asymmetric dimeric acceptors **PDI-TPDI** and **PDI-SePDI** were determined by $^1$H NMR (Fig. S1–S6 and S8, ESI†). It was noted that, S-annulation made the chemical shifts of the aromatic hydrogen increase during the $^1$H NMR spectra of TPDI and **TPDIBr** (Fig. S1 and S2, ESI†) compared with those of the unfused PDI-HD and its monobromide PDI-HDBr.[49] Furthermore, the corresponding chemical shifts of the aromatic hydrogens of SePDI and mono-brominated **SePDIBr** were slightly increased (Fig. S3 and S4, ESI†). The reason was likely due to an enhanced deshielding effect (triggered by the anisotropy of the enlarged conjugated aromatic rings) as a result of

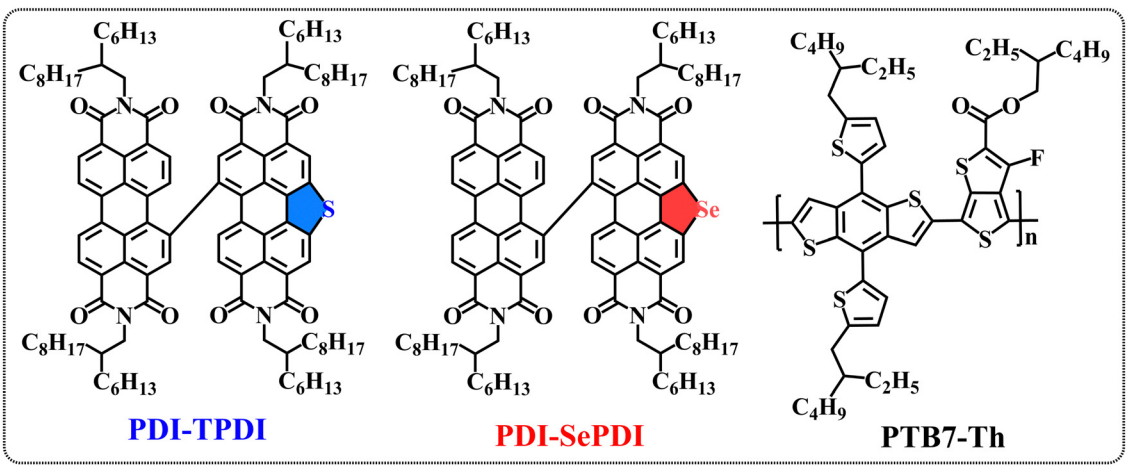


Chart 1 Chemical structure of the studied asymmetric S/Se-annulated dimers **PDI-TPDI** and **PDI-SePDI** and donor **PTB7-Th** in this study.

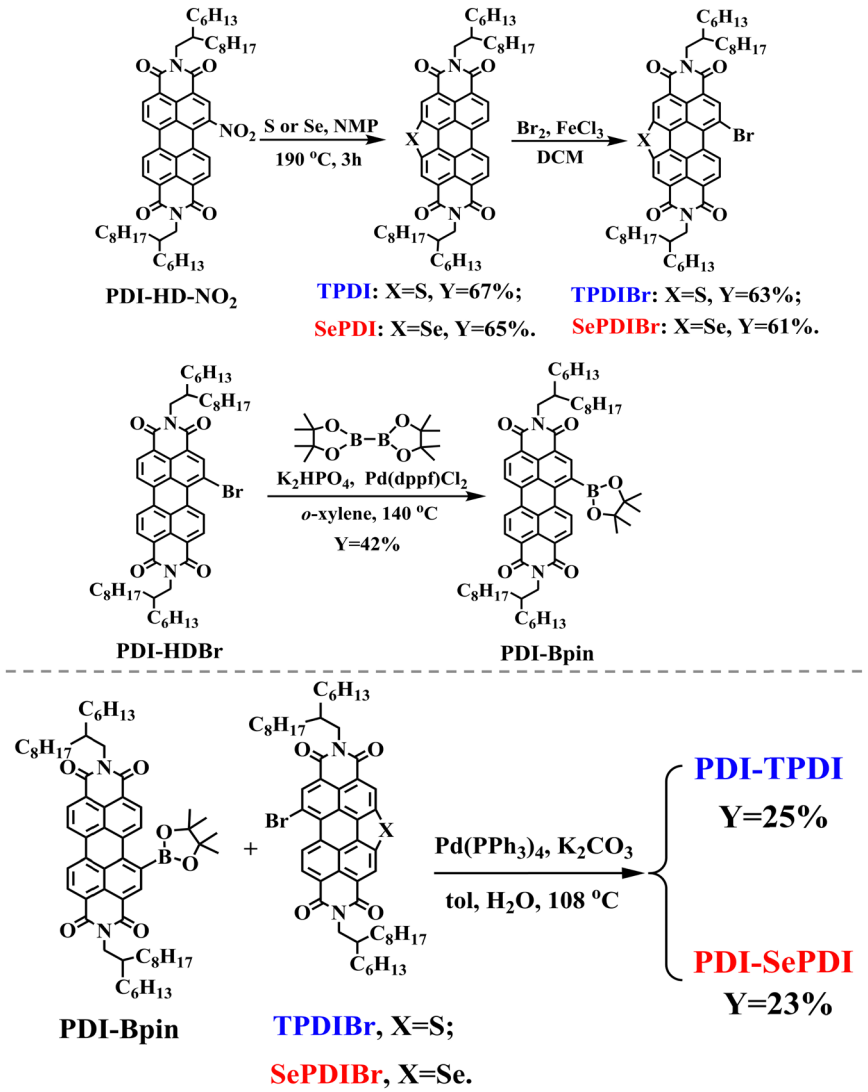


Scheme 1 Synthesis of monobromides **TPDIBr** and **SePDIBr**, monoboric ester **PDI-Bpin** and asymmetric PDI dimeric acceptors **PDI-TPDI** and **PDI-SePDI**.

introducing the Se atom with its bigger and looser outermost electron cloud compared to that of the S atom, and the latter DFT calculation excluded the steric effect. For S-annulation **PDI-TPDI**, chemical shifts ranging from 9.52 to 7.84 ppm belonged to the hydrogens of unfused PDI and S-annulated TPDI aromatic rings, one in the range of 4.13–3.98 ppm was attributed to hydrogens of methylene directly linked to imide N, one ranging from 1.98 to 1.87 ppm was ascribed to the hydrogens of methane, and the remainder were assigned to hydrogens of $-CH_2-$ and $-CH_3$ groups (Fig. S6, ESI†). Because of the stronger deshielding effect of the newly formed selenophene ring, the chemical shifts were all slightly increased and moved forward the low field (Fig. S8, ESI†). The structures of the designed asymmetric dimeric acceptors S-annulation **PDI-TPDI** and Se-annulation **PDI-SePDI** were further characterized by the $^{13}C$ NMR spectra (Fig. S7 and S9, ESI†).

Both asymmetric acceptors exhibited excellent solubility in chlorobenzene (CB) and chloroform (CF) solvents. As shown in Fig. 1a, the thermal decomposition temperatures ($T_d$, 5% weight-loss) were observed to be 426 °C for **PDI-TPDI** and 409 °C for **PDI-SePDI**, determined by thermogravimetric analysis (TGA) in the nitrogen atmosphere. The observed 17 °C decreased $T_d$ could be interpreted by the weakened solid molecular stacking interaction found in the later XRD measurement. Overall, the exhibited $T_d$ higher than 400 °C indicated that both asymmetric **PDI-TPDI** and **PDI-SePDI** possessed excellent thermo-stability during the fabrication procedure of OSCs.

## Optical properties, photostability, aggregation and energy levels

The normalized UV-Vis absorption spectra for **PDI-TPDI** and **PDI-SePDI** both in diluted $CH_2Cl_2$ solution and film were implemented in order to investigate the light absorption properties during these asymmetric NFEAs. The obtained results are shown in Fig. 1b, c and Table 1. Two asymmetric acceptors

 

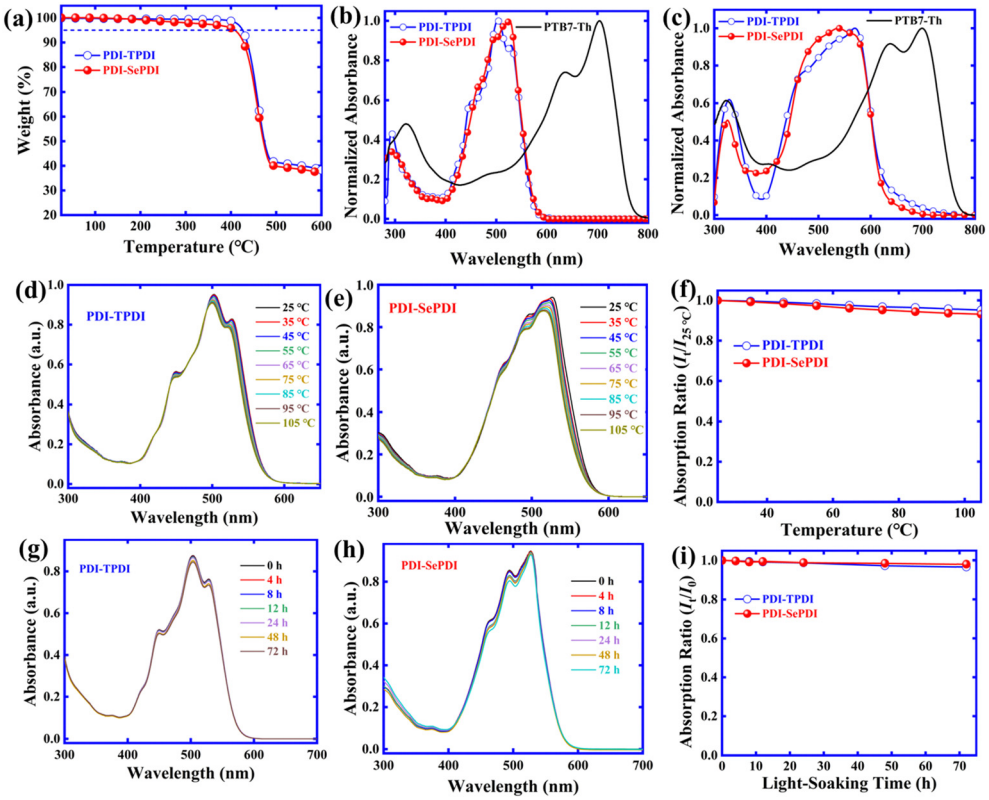


Fig. 1 TG curve for asymmetric acceptors **PDI-TPDI** and **PDI-SePDI** (a), absorption in dilute $CH_2Cl_2$ (b) and as neat films (c), temperature-dependent absorption for **PDI-TPDI** (d) and **PDI-SePDI** (e) as well as the curve of maximum absorption intensity relative to temperature (f), changes for UV-vis absorption for **PDI-TPDI** (g) and **PDI-SePDI** (h) in chlorobenzene after illumination, and absorption intensity variation trend relative to light-soaking time (i).

Table 1 Optical and electrochemical data for the asymmetric acceptors **PDI-TPDI** and **PDI-SePDI**

| | Solution | | Film | | | | | | | | |
|---|---|---|---|---|---|---|---|---|---|---|---|
| Material | $\lambda_{max}$ (nm) | $\lambda_{sh}$ (nm) | $\lambda_{max}$ (nm) | $\lambda_{sh}$ (nm) | $\lambda_{onset}$ (nm) | $E_g^{opt\,a}$ (eV) | $\varphi_{ox}^{onset}$ (V) | $\varphi_{red}^{onset}$ (V) | $E_{HOMO}{}^{b}$ (eV) | $E_{LUMO}{}^{c}$ (eV) | $E_g^{ec\,d}$ (eV) |
| **PDI-TPDI** | 293, 503 | 448, 529 | 329, 570 | 471 | 633 | 1.96 | 1.68 | −0.86 | −6.38 | −3.84 | 2.54 |
| **PDI-SePDI** | 288, 526 | 464, 498 | 325, 538 | 570 | 625 | 1.98 | 1.58 | −0.81 | −6.28 | −3.89 | 2.39 |
| **PTB7-Th** | 321, 705 | 636 | 323, 698 | 636 | 761 | 1.63 | 0.53 | −1.13 | −5.23 | −3.57 | 1.66 |

[a] Estimated from the absorption onset of the asymmetric acceptors in the film ($E_g^{opt} = 1240/\lambda_{onset}^{film}$). [b] Obtained from the oxidation potential for asymmetric acceptors ($E_{HOMO} = -e(\varphi_{ox}^{onset} - \varphi_{ox}^{Fc} + 4.80)$ (eV)). [c] Calculated from the reduction potential for asymmetric acceptors ($E_{LUMO} = -e(\varphi_{red}^{onset} - \varphi_{ox}^{Fc} + 4.80)$ (eV)). [d] Calculated from $E_g^{ec} = -(E_{HOMO} - E_{LUMO})$ (eV).

**PDI-TPDI** and **PDI-SePDI** possessed a wide absorption in the wavelength range of 400–600 nm, which was similar to the absorption profile with the symmetric analogues di-PBI[36] and SdiPBI-S.[39] As for S-annulated **PDI-TPDI**, absorption peaks at 293 and 503 nm together with one high energy shoulder peak at 448 nm and one low energy shoulder peak at 529 nm in diluted $CH_2Cl_2$ solution were found, whilst absorption peaks at 288 and 526 nm and two high-energy shoulder peaks at 464 and 498 nm in **PDI-SePDI** were found. The chlorobenzene solution state molar extinction coefficient ($\varepsilon$) for these studied asymmetric acceptors was further measured, as exhibited in Fig. S10 (ESI†). It was elucidated that the values of ε were in turn calculated to be $6.71 \times 10^4$ $M^{-1}$ $cm^{-1}$ at 503 nm for **PDI-TPDI** and $5.52 \times 10^4$ $M^{-1}$ $cm^{-1}$ at 526 nm for **PDI-SePDI** (Table S1, ESI†), indicating a slightly decreased ε in Se-annulation **PDI-SePDI**. What is more, moving from solution to film, the large red-shift of approximately 36 nm from 293 nm to 329 nm and 67 nm from 503 nm to 570 nm together with a high-energy shoulder peak at 471 nm were found in S-annulation **PDI-TPDI**, while after applying the larger atomic radius Se-annulation **PDI-SePDI**, the red-shifted value of 37 nm from 288 nm to 325 nm and 12 nm from 526 nm to 538 nm as well as the low-energy shoulder peak at 570 nm were found. The close red-shift value of high energy peak but significantly small red-shift value of the low energy peak indicated that the Se-annulation **PDI-SePDI** possessed the weak aggregation.[50] Interestingly, the **PDI-SePDI** had a stronger absorption ranging from

450–580 nm than that of **PDI-TPDI**. Moreover, **PDI-TPDI**- and **PDI-SePDI**-based films exhibited absorption band edges ($\lambda_{onset}^{film}$) of 633 and 625 nm, corresponding to the optical bandgaps ($E_g^{opt}$) of 1.96 and 1.98 eV, respectively, which were slightly smaller than their symmetric analogues.[36,39]

The fluorescence spectra of the two asymmetric acceptors **PDI-TPDI** and **PDI-SePDI** in diluted dichloromethane (DCM) solution and film states were also measured in Fig. S11 (ESI†). The excitation wavelength ($\lambda_{ex}$) was situated at 503 nm in DCM and 480 nm in the film for **PDI-TPDI**, whereas the $\lambda_{ex}$ was placed at 480 nm in DCM and 538 nm in film for **PDI-SePDI**. The S-annulated **PDI-TPDI** exhibited the emission peak at 584 nm in DCM solution and 628 nm in film, in contrast, Se-annulated **PDI-SePDI** showed the distinctive dual peaks at 532 nm and 575 nm as well as 634 nm in film (Table S1, ESI†).

The solution aggregation behaviour was estimated by applying the temperature-dependent absorption (TD-Abs)[45,51] and the related results are shown in Fig. 1. We can see that when the temperature is heated from 25 °C to 105 °C with 10 °C as an interval in CB solution, a 3-nm blue-shift from 503 nm to 500 nm and a 4.64% decreased absorption intensity from 0.9528 to 0.9086 of the maximum peak, as well as a 7-nm blue-shift from 527 nm to 520 nm and 5.07% decreased intensity from 0.8287 to 0.7867 of the low-energy shoulder peak are observed in **PDI-TPDI** (Fig. 1d). Meanwhile, the 11-nm blue-shift from 526 nm to 515 nm and 7.07% decreased absorption intensity from 0.9405 to 0.8740 of the maximum peak, as well as the 5-nm blue-shift from 498 nm to 493 nm and 8.52% decreased intensity from 0.8620 to 0.7886 of the high-energy shoulder peak are observed in **PDI-SePDI** (Fig. 1e). The observed larger blue-shifted value for the maximum absorption peak and more significant decreased value of intensity suggested that Se-annulated **PDI-SePDI** possessed relatively weaker solution aggregation (Fig. 1f).[22,52]

The photostability of these resultant asymmetric small molecular acceptors **PDI-TPDI** and **PDI-SePDI** and the influence of the different annulation method at the outer bay positions were evaluated in Fig. 1. As for **PDI-TPDI**, the maximum peak slightly changed and the intensity was decreased by 96.51%, and the bilateral shoulder peaks exhibited 96.26% and 96.16% decreased intensity, while **PDI-SePDI** exhibited a relatively smaller intensity decrease (98.31%) and the shoulder peaks exhibited 92.16% and 94.76% decreased intensity, after exposing the light for 72 h in CB solution. These observations demonstrated that these asymmetric acceptors **PDI-TPDI** and **PDI-SePDI** both had high photostability in solution state (Fig. 1i). This attractive photostability was also observed in these PDI dimeric molecules 2T-(PDI-HD)$_2$ with bithiophene (2T) as linker and F2T-(PDI-HD)$_2$ with fluorinated 2T (F2T) as linker,[41] and outer bay N-annulated dimers with high charge mobility TVT and TYT as linkers,[21] as well as A–A type PDI-containing polymer acceptors (PAs).[23]

The molecular stacking interaction and solid aggregation as well as the influence of different annulation types were estimated by the X-ray diffraction (XRD) analyses, as indicated in Fig. S12 (ESI†). The **PDI-TPDI**-based film exhibited a sharp and strong peak at $2\theta$ = 3.99°, while the **PDI-SePDI**-based film exhibited a very weak peak at $2\theta$ = 3.77°, corresponding to the inter-chain stacking distance of 22.12 Å and 23.41 Å, respectively. Unfortunately, no obvious diffraction peaks in the large angle region were found in the resultant asymmetric PDI small molecular acceptors.[53] The enlarged inter-chain stacking distance in Se-annulated **PDI-SePDI** suggested the presence of degraded solid stacking interactions, which is in agreement with the smaller red-shift value from solution to film state and relatively weaker solution aggregation from TD-Abs analysis.

## Electrochemical properties

To know the energy level information of the asymmetric dimeric acceptors and the impact of different annulation methods, the cyclic voltammetry (CV) method was applied to measure the electrochemical properties of these resulting asymmetric PDI acceptors. Note that the redox couple ($\varphi_{1/2}$) for Fc/Fc$^+$ was 0.10 V relative to the Ag/AgNO$_3$ reference electrode.[54] As can be seen from Fig. 2a and Table 1, the oxidation onset potential ($\varphi_{ox}^{onset}$) and reduction onset potential ($\varphi_{red}^{onset}$) in the film state were separately found to be 1.68 V and −0.86 V for S-annulated **PDI-TPDI**, together with 1.58 V and −0.81 V for Se-annulated **PDI-SePDI**. Thereupon, the corresponding $E_{HOMO}$, $E_{LUMO}$ and electrochemical band gap ($E_g^{ec}$) were in sequence estimated to be −6.38, −3.84 and 2.54 eV for S-annulated **PDI-TPDI** and −6.28, −3.89 and 2.39 eV for Se-annulated **PDI-SePDI**.[51] The LUMO values of these asymmetric **PDI-TPDI** and **PDI-SePDI** were close to those of the symmetric analogues (−3.85 eV for SdiPBI-S and −3.87 eV SdiPBI-Se).[16,39] Clearly, after applying Se-annulation, the 0.05 eV down-shifted $E_{LUMO}$ from −3.84 to −3.89 eV was observed. Furthermore, we found that there existed the 0.27–0.32 eV LUMO energy offset between **PTB7-Th** and these studied asymmetric acceptors **PDI-TPDI** and **PDI-SePDI**, which could guarantee the high-performance exciton dissociation.[41,55]

## Theoretical calculations

In order to clarify the internal configuration and the influence of modulation of different annulation on the molecular twisting degree, theoretical calculations were carried out using density-functional theory (DFT) at the B3LYP/6-311G(d,p) level (Gaussian 09).[56] For predigesting the calculations and saving time, considering that the flexible 2-hexyldecyl (HD) side chain

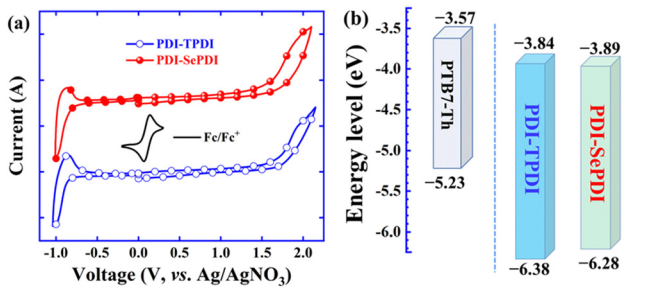


Fig. 2 CV curves of asymmetric acceptors **PDI-TPDI** and **PDI-SePDI** (a) and energy level alignment for the used donor and acceptors (b).

 

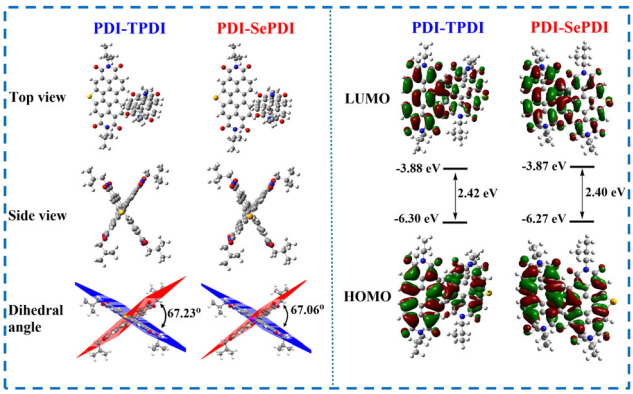


Fig. 3 Top-/side-view of the optimized molecular structures, HOMO/LUMO orbital distributions and the calculated energy levels for model compounds **PDI-TPDI** and **PDI-SePDI**.

played a negligible effect on electron distribution and energy level, the HD group of these resulting asymmetric acceptors **PDI-TPDI** and **PDI-SePDI** at the imide position was replaced with the iso-butyl ($^{i}$Bu) group. As presented in Fig. 3, during these **PDI-TPDI** and **PDI-SePDI** model molecules, the electron clouds of HOMO and LUMO orbitals were distributed across the whole aromatic skeleton, leading to the large band gap of 2.40–2.42 eV. Also, the $E_{HOMO}$ and $E_{LUMO}$ values were −6.30 eV and −3.88 eV for **PDI-TPDI**, respectively, after Se-annulation, the corresponding values were in turn moved to −6.27 eV and −3.87 eV. After replacing S-annulation with Se-annulation, the $E_{HOMO}$ was increased by 0.30 eV, the $E_{LUMO}$ was up-shifted by 0.01 eV, and the bandgap was reduced by 0.02 eV, which was similar to the results obtained in the CV test. Interestingly, the dihedral angle between the PDI ring and the heteroatom S/Se-annulation aromatic ring were in turn calculated to be 67.23° for **PDI-TPDI** and 67.06° for **PDI-SePDI** (Fig. 3). Moreover, the values of the torsion angle ($\theta$) between the PDI ring and S/Se-annulated PDI rings were found to be 107.98° for **PDI-TPDI** and 108.19° for **PDI-SePDI** (Table S2, ESI†). In addition, the dihedral angle between the PDI ring and heterocyclic ring during the heteroatom-annulated PDI subunit was found to be 1.59° for **PDI-TPDI** and 1.57° for **PDI-SePDI**, respectively (Fig. S13, ESI†), indicating the presence of similar steric hindrance. These close dihedral angles and torsion angles suggested the different annulation methods played a negligible effect on the molecular twisting degree. The dipole moment of these asymmetric acceptors was found to be 0.8891 Debye for **PDI-TPDI** and 0.3827 Debye for **PDI-SePDI**, respectively.

To gain further insight into the impact of different annulation types on the molecular surface electrostatic potential (ESP) and ESP area distributions, the corresponding theoretical calculations were performed.[57,58] As can be seen from Fig. S14 (ESI†), the negative region was principally distributed on the oxygen of the imide from fused TPDI/SePDI and unfused PDI aromatic rings. After replacing S-annulation with Se-annulation, the molecular polarity index (MPI) was decreased from 8.96 kcal mol$^{-1}$ to 8.90 kcal mol$^{-1}$, while the overall average ESP was also descended from 2.85 kcal mol$^{-1}$ to 2.71 kcal mol$^{-1}$. The difference of the overall average ESP between donor and acceptor was reduced from 4.46 kcal mol$^{-1}$ of the (TB7-Th)$_2$:**PDI-TPDI** system to 4.32 kcal mol$^{-1}$ of the (TB7-Th)$_2$:**PDI-SePDI** system (Table S3, ESI†), indicating the presence of reduced intermolecular interaction.[59] Fig. S14b (ESI†) exhibited that **PDI-TPDI** possessed a wider ESP distribution range. The Se-annulation made the overall surface area increase from 927.35 Å$^2$ to 931.09 Å$^2$, which benefited from annulation of the larger Se atom in **PDI-SePDI**.

## Photovoltaic properties

In order to understand the solar cell performance of these studied asymmetric acceptors and clarify the influence of different annulation methods in **PDI-TPDI** and **PDI-SePDI**, devices adopting the traditional structure (ITO/PEDOT:PSS/**PTB7-Th**:asymmetric acceptors/PDINO/Al) were fabricated. The detailed testing process embodied screening the weight ratio of D/A, utilizing the high boiling point 1,8-diiodooctane (DIO) solvent additive and thermal annealing (TA) at 110 °C for 10 min and so on. As for S-annulation **PDI-TPDI**, the D:A ratios (from 1 : 1.2 to 1 : 1 then to 1.2 : 1) were tested, and it was found that the best weight ratio was 1 : 1. Meanwhile, for the Se-annulation **PDI-SePDI**, the weight ratio was varied from 1 : 1.5 to 1 : 1.8 then to 1 : 2, and the optimal weight ratio was 1 : 1.8 (Fig. S15 and Table S4, ESI†). Under the conditions of each best D:A ratio, **PDI-TPDI** exhibited the $V_{OC}$ of 0.72 V, a $J_{SC}$ of 7.02 mA cm$^{-2}$ and a high FF of 61.34%, leading to the PCE of 3.10%. After utilizing Se-annulation, the **PDI-SePDI**-based device afforded the $V_{OC}$ of 0.71 V, the 52.85% increased $J_{SC}$ of 10.73 mA cm$^{-2}$, and the decreased FF of 45.83%, resulting in the 12.90% enhanced PCE of 3.50%. Since the DIO could tune the morphology of the photoactive layer in the OSCs and form the interpenetrating network BHJ structure with nano-sized phase separation, 3% DIO was applied aiming to boost the PV performance.[23,51] After the 3% DIO was applied, the **PDI-TPDI**-based device afforded the unchanged $V_{OC}$ of 0.72 V, the 39.17% decreased $J_{SC}$ of 4.27 mA cm$^{-2}$, and the 24.73% down-shifted FF of 46.17%, leading to the 53.87% dropped PCE of 1.43%. Meanwhile, the **PDI-SePDI**-based device yielded the slightly decreased $V_{OC}$ of 0.70 V, 51.54% reduced $J_{SC}$ of 5.20 mA cm$^{-2}$, and 23.78% upshifted FF of 56.73%, producing the 40.86% dropped PCE of 2.07% (Fig. S16 and Table S4, ESI†). Unfortunately, the DIO solvent additive had a negative impact on solar cell performance and never elevated the photovoltaic performance. Considering the optimization of the morphology and thus promotion of the PV performance of thermal annealing, the TA at 110 °C for about 10 min was further applied.[21,60] When using TA treatment, the S-annulation **PDI-TPDI**-based device gained the stable $V_{OC}$ of 0.72 V, the 33.76% increased $J_{SC}$ of 9.39 mA cm$^{-2}$, and the 18.31% decreased FF of 50.11%, contributing to the 9.4% elevated PCE of 3.39%. In the meantime, the Se-annulation **PDI-SePDI** gained the slightly decreased $V_{OC}$ of 0.70 V, the 36.44% elevated $J_{SC}$ up to 14.64 mA cm$^{-2}$, and the 13.11% enhanced FF of 51.84%, giving rise to the 51.71% up-shifted PCE as high as 5.31% (Fig. S16 and Table S4, ESI†).

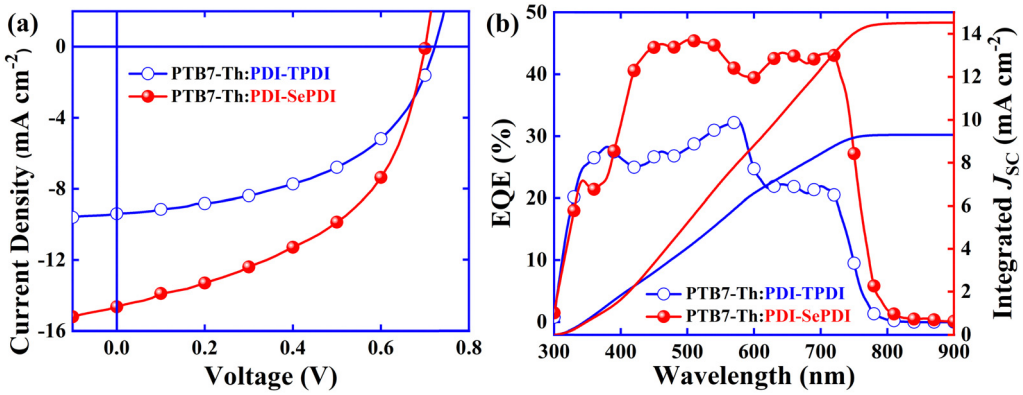


Fig. 4 Best *J*–*V* (a) and EQE (b) curves for **PDI-TPDI** and **PDI-SePDI**-based devices.

Table 2 A summary of the photovoltaic parameters of **PDI-TPDI** and **PDI-SePDI**-based devices

| Acceptor | Conditions | $V_{OC}$ (V) | $J_{SC}$[a] (mA cm$^{-2}$) | FF (%) | PCE[b] (%) | $R_{SH}$ (Ωm$^2$) | $R_S$ (Ωm$^2$) |
|---|---|---|---|---|---|---|---|
| **PDI-TPDI** | 1 : 1/TA | 0.72 ± 0.01 | 9.39 ± 0.08 (9.30) | 50.11 ± 0.43 | 3.39 ± 0.13 | 435.97 | 11.14 |
| **PDI-SePDI** | 1 : 1.8/TA | 0.70 ± 0.01 | 14.64 ± 0.22 (14.52) | 51.84 ± 0.38 | 5.31 ± 0.24 | 137.02 | 6.47 |

[a] Integrated $J_{SC}$ calculated from EQE. [b] Statistics in parentheses from 10 independent cells.



Going through a series of device optimizations, the best current density relative to voltage curves and corresponding EQE spectra are exhibited in Fig. 4. It was found that, under optimal conditions, S-annulation **PDI-TPDI**-based device exhibited a $V_{OC}$ of 0.72 V, a $J_{SC}$ of 9.39 mA cm$^{-2}$, an FF of 50.11% and thus a PCE of 3.39%, after Se-annulation, **PDI-SePDI** achieved the slightly decreased $V_{OC}$ of 0.70 V, the 55.91% increased $J_{SC}$ up to 14.64 mA cm$^{-2}$, the 3.45% enhanced FF of 51.84% and thus the 56.64% elevated PCE as high as 5.31%. The marked increase in $J_{SC}$ was verified by the enhancement of EQE ranging from 400 nm to 750 nm (Fig. 7b) and slightly enhanced FF was explained by the downgraded series resistance ($R_S$) from 11.14 Ω m$^2$ to 6.47 Ω m$^2$ (Table 2). Additionally, based on the EQE spectra, the integrated $J_{SC}$ was in sequence calculated to be 9.30 and 14.52 mA cm$^{-2}$, exhibiting a tolerable error of less than 5%, indicative of the high creditability of photocurrent measured from the *J*–*V* test. Additionally, the corresponding device stability was estimated in Fig. S17 (ESI†).[23] When the light exposure lasted for 72 h, the devices parameters $V_{OC}$, $J_{SC}$, FF and PCE remained approximately 98%, 88%, 91% and 79% of their initial values, suggesting that these asymmetric PDI dimers exhibited relatively higher stability.

### Exciton dissociation, recombination and charge transport properties

To deeply understand the reason for the Se-annulated **PDI-SePDI**-based device obtaining the higher $J_{SC}$ and determine the impact of different annulation methods on dissociation and collection procedure of excitons, photocurrent ($J_{ph}$) *versus* effective voltage ($V_{eff}$) was measured in Fig. 5a and b. The $J_{ph}$ reached the saturated value ($J_{sat}$) of 9.32 mA cm$^{-2}$ for **PDI-TPDI** and 14.56 mA cm$^{-2}$ for **PDI-SePDI** when $V_{eff}$ was larger than 2.50 V. The exciton dissociation probability ($\eta_{diss}$) was calculated to be 81.9% for **PDI-TPDI** and 89.7% for **PDI-SePDI**, meanwhile, the charge collection probability ($\eta_{coll}$) was in turn found to be 71.4% for **PDI-TPDI** and 70.6% for **PDI-SePDI** (Table 3). Obviously, the increased $\eta_{diss}$ and close $\eta_{coll}$ could partially account for the 55.91% increased $J_{SC}$ and slightly elevated FF.[61]

$J_{SC}$ relative to light intensity ($P_{light}$) tests were conducted to investigate the biomolecular recombination behaviors of these resultant asymmetric acceptors (Fig. 5c and d). The $J_{SC}$ and $P_{light}$ obeyed the power law equation of $J_{SC} \propto (P_{light})^{\alpha}$, where the value of $\alpha$ (slope of the fitting line) approaching to 1 implied a low bimolecular recombination.[23,61,62] The $\alpha$ values of 0.927 for **PDI-TPDI** and 0.986 for **PDI-SePDI** were observed in short-circuit conditions, which is indicative of the suppressed bimolecular recombination after Se-annulation (Fig. 5c). Furthermore, the monomolecular or trap-assisted recombination behavior was further evaluated *via* testing the variation of $V_{OC}$ with respect to $P_{light}$, as depicted in Fig. 5d. The $V_{OC}$ relative to $P_{light}$ relationship was described as $V_{OC} \propto (nK_BT/q)\ln(P_{light})$, in which $K_B$, $T$ and $q$ stand for Boltzmann constant, absolute temperature and elementary charge, respectively. Note that the slope of $nK_BT/q$ was equal to $k_BT/q$, indicating that bimolecular recombination was dominant, while $nK_BT/q$ was close to $2k_BT/q$, which implied that monomolecular or trap-assisted recombination took place. It was exhibited that the n values were separately found to be 1.91 for **PDI-TPDI** and 1.32 for **PDI-SePDI**, suggesting that the suppressed monomolecular or trap-assisted recombination mechanism played a dominant role in the **PDI-SePDI**-based device.[63] Apparently, the suppressed bimolecular- and monomolecular- and/or trap-assisted recombination could in part explain why the **PDI-SePDI**-based device acquired the increased $J_{SC}$ and thus enhanced PCE.

To find out the origin why **PDI-SePDI**-containing devices obtained a significantly enhanced $J_{SC}$ and slightly elevated FF

 

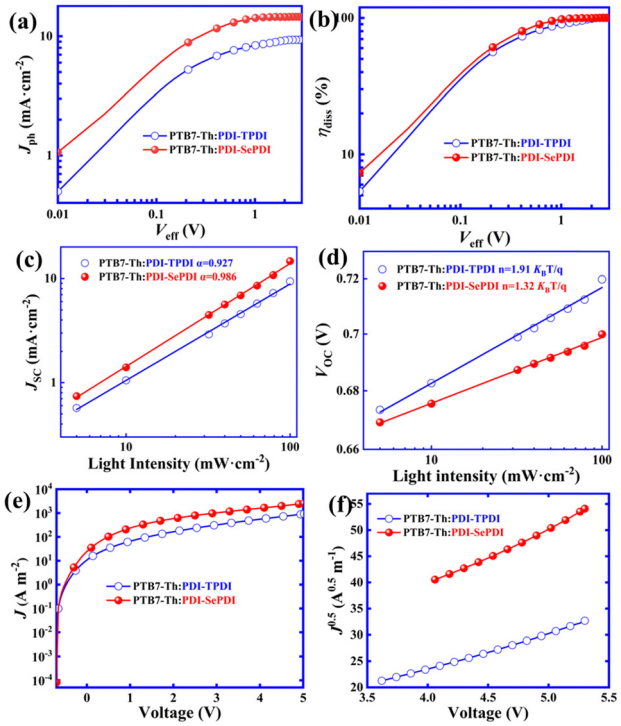


Fig. 5 Plots of $J_{ph}$ *vs.* effective voltage ($V_{eff}$) (a), $\eta_{diss}$ *vs.* $V_{eff}$ (b), $J_{SC}$ *vs.* light intensity (c), $V_{OC}$ *vs.* light intensity (d), *J*–*V* curve (e) and fitting $J^{0.5}$–*V* curve (f) for **PDI-TPDI** and **PDI-SePDI**-based devices.

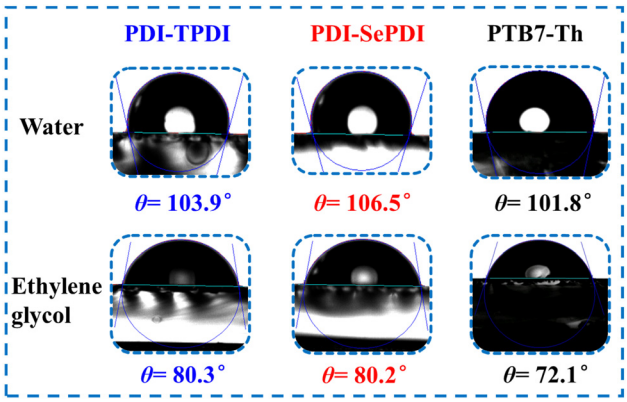


Fig. 6 Contact angle on **PDI-TPDI**, **PDI-SePDI** and **PTB7-Th** films.

and to determine the impact of different annulation methods at the bay position of PDI, the space-charge-limited-current (SCLC) electron mobility ($\mu_e$) was measured applying the vertical electron-only devices in the structure of ITO/ZnO/**PTB7-Th**:**PDI-TPDI** or **PDI-SePDI**/PDINO/Al (Section 1.3 in ESI†).[51,64] Note that the thickness values of these resultant asymmetric acceptors **PDI-TPDI** and **PDI-SePDI** based films were found to be 100 nm and 105 nm, respectively. Obviously, after utilizing the Se-annulation to replace S-annulation, the $\mu_e$ value was increased from $1.24 \times 10^{-5}$ $cm^2$ $V^{-1}$ $s^{-1}$ to $3.98 \times 10^{-5}$ $cm^2$ $V^{-1}$ $s^{-1}$ (Fig. 5e, f and Table 3). The 3.21-fold elevated electron mobility could in part explain the origin of the 55.91% elevated $J_{SC}$ and 3.45% elevated FF in the **PDI-SePDI**-based device.

### Morphology characteristics of the active layers

To further understand the influence of different annulation methods on miscibility and interaction between **PTB7-Th** and **PDI-TPDI**/**PDI-SePDI**, we measured the corresponding contact angle (CA), and the related parameters including contact angles ($\theta$), surface tension ($\gamma$), and surface energy parameters ($\chi$), which are listed in Table S6 (ESI†). As can be seen from Fig. 6, the $\gamma$ values of the used electron donor **PTB7-Th**, and the resultant asymmetric acceptors **PDI-TPDI** and **PDI-SePDI** in the pristine films were separately estimated to be 29.65, 20.53 and 23.47 mN $m^{-1}$. Then, the Flory–Huggins interaction parameter $\chi^{D-A}$ was calculated from the formula, $\left(\chi^{D-A} = K\left(\sqrt{\gamma_{donor}} - \sqrt{\gamma_{acceptor}}\right)^2\right)$ to be 0.863K for **PTB7-Th**:**PDI-TPDI** combination and 0.361K for **PTB7-Th**:**PDI-SePDI** system.[49,65] Apparently, replacing S-annulation with Se-annulation in the **PTB7-Th**:**PDI-SePDI** system resulted in the decreased $\chi^{D-A}$, suggesting that **PDI-SePDI** showed the enhanced miscibility with donor **PTB7-Th**, which was helpful to form the advantageous morphology. This correlated well with the following observed relatively smoother surface after Se-annulation.

To deeply figure out the reason why the Se-annulation **PDI-SePDI**-based device obtained the significantly increased $J_{SC}$ and slightly enhanced FF and the influence of different annulation on surface morphology, the tapping-model AFM was applied, as depicted in Fig. 7a–d. After utilizing Se-annulation **PDI-SePD** instead of S-annulation **PDI-TPDI**, the values of the root-mean-square (RMS) was decreased from 2.452 nm to 2.293 nm. Furthermore, we further measured the scanning electron microscopy (SEM) images in Fig. 7e and f. A smoother surface was found in the Se-annulated **PTB7-Th**:**PDI-SePDI**-based blend film. The observed reduced surface roughness and flattened blend film was in accordance with the weakened aggregation both in the CB solution and film states and the improved miscibility with **PTB7-Th** obtained from the CA measurement.

Table 3 A summary of exciton dissociation, charge collection and mobility in **PDI-TPDI**- and **PDI-SePDI**-based devices

| Acceptor | $J_{sat}$ [a] (mA $cm^{-2}$) | $J_{ph}^{s}$ [b] (mA $cm^{-2}$) | $J_{ph}^{m}$ [c] (mA $cm^{-2}$) | $\eta_{diss}$ [d] (%) | $\eta_{coll}$ [e] (%) | $\mu_e$ ($cm^2$ $V^{-1}$ $s^{-1}$) |
|---|---|---|---|---|---|---|
| **PDI-TPDI** | 9.32 | 7.63 | 6.65 | 81.9 | 71.4 | $1.24 \times 10^{-5}$ |
| **PDI-SePDI** | 14.56 | 13.06 | 10.28 | 89.7 | 70.6 | $3.98 \times 10^{-5}$ |

[a] Saturated photocurrent density. [b] Photocurrent density at short-circuit condition. [c] Photocurrent density at maximal power output. [d] $\eta_{diss} = J_{ph}^{s}/J_{sat}$. [e] $\eta_{coll} = J_{ph}^{m}/J_{sat}$.

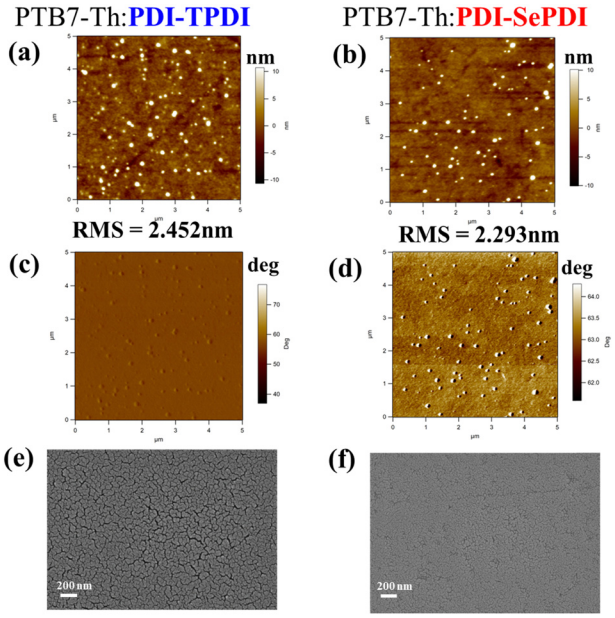


Fig. 7 AFM height images with (a) and (b), phase images with (c) and (d) and SEM images (e) and (f) for **PDI-TPDI**- (a), (c) and (e) and **PDI-SePDI**-containing (b), (d) and (f) blend films.

The improved morphology could in part account for the 3.21-times increased electron mobility, the 55.91% elevated photocurrent and thus the 56.64% enhanced photovoltaic efficiency.[66,67] We also observed the presence of some bulges during these resultant asymmetric **PDI-TPDI** and **PDI-SePDI**-based photoactive layers which did not favour formation of the desired microstructural morphology and thus restricted the device performance. There was still some room for the morphology optimization of the photoactive layer, so more solvent additives and post-treatment could be adopted in future work.

## Conclusions

To sum up, two asymmetric PDI-based dimeric acceptors, named **PDI-TPDI** and **PDI-SePDI**, were developed by heteroatom S/Se-annulation at the outside position of a PDI aromatic ring. The resultant asymmetric acceptors exhibited outstanding thermo- and photo-stability as well as a similar dihedral angle of 67° between two PDI planes. Replacing S-annulation with Se-annulation led to a blue-shifted maximal absorption peak, weakened aggregation both in solution and solid film states, and deepening of the $E_{LUMO}$ energy level, as well as having an inconsequential effect on the twisting angle between the PDI and S/Se-annulation aromatic rings. Thereupon, the S-annulated **PDI-TPDI**-based device obtained the $V_{OC}$ of 0.72 V, $J_{SC}$ of 9.39 mA cm$^{-2}$, and FF of 50.11%, giving rise to the PCE of 3.39%, while Se-annulated **PDI-SePDI** achieved the slightly decreased $V_{OC}$ of 0.70 V, the increased $J_{SC}$ of 14.64 mA cm$^{-2}$ and FF of 51.84%, contributing to a 56.64% elevated PCE up to 5.31%. The increase of PCE in the **PDI-SePDI**-containing device principally benefited from the enhanced exciton dissociation, suppressed charge recombination, and increased charge mobility originating from the advantageous microstructural morphology generated by larger heteroatom Se-annulation. The structure–property–performance relationship study proved that Se-annulation of PDI at the outside position was an effective strategy for tuning the molecular aggregation, morphology and further boosting the solar cell performance.

## Experimental section

### Materials

Chemical reagents used in this work were obtained from commercial companies. Starting material mononitrated PDI-HD-$NO_2$[21] and monobromide PDI-HDBr[49] were synthesized according to the corresponding method. The synthetic details for the used key monobromides **TPDIBr**, **SePDIBr** and monoborate ester **PDI-Bpin** can be found in the ESI.†

**Synthesis of 6-(*N*,*N*′-bis(2-hexyldecyl)perylenediimide-1-yl)-[1,12-*b*,*c*,*d*]thiophene-*N*,*N*′-bis(2-hexyldecyl)perylenediimide (PDI-TPDI).** Under Ar, a mixture of **PDI-Bpin** (70.0 mg, 0.073 mmol), **TPDIBr** (76.1 mg, 0.080 mmol, 1.1 eq.), $K_2CO_3$ (27.6 mg, 0.2 mmol), 5 mL degassed toluene, 0.1 mL $H_2O$, and $Pd(PPh_3)_4$ (7 mg, 0.0061 mmol) was added into a 25-mL double-neck flask. The resulting solution was kept under reflux for about 24 h. After cooling to room temperature (RT), the solution was poured into $H_2O$ and extracted with $CH_2Cl_2$. Next, the organic phase was washed with $H_2O$ then dried with anhydrous $Na_2SO_4$. After removing the solvent, the crude product was purified by column chromatography (PE : $CH_2Cl_2$ = 1 : 1) as the eluent to acquire 34 mg **PDI-TPDI** as a red solid (yield = 25%). M.p. > 280 °C. $^1$H NMR (500 MHz, $CDCl_3$), $\delta$ (ppm): 9.51 (s, 1H, H of PDI), 9.43 (s, 1H, H of PDI), 8.89–8.83 (m, 2H, H of PDI), 8.76 (s, 2H, H of PDI), 8.59 (d, $^3J$ = 8.5 Hz, 1H, H of PDI), 8.53 (s, 1H, H of PDI), 8.48 (s, 1H, H of PDI), 8.44 (d, $^3J$ = 8.5 Hz, 1H, H of PDI), 8.12 (d, $^3J$ = 8.5 Hz, 1H, H of PDI), 7.84 (d, $^3J$ = 8.5 Hz, 1H, H of PDI), 4.13 (d, $^3J$ = 6.5 Hz, 4H, >N–$CH_2$–), 4.06 (d, $^3J$ = 6.5 Hz, 2H, >N–$CH_2$–), 3.98 (br, 2H, >N–$CH_2$–), 1.98 (br, 2H, >CH–), 1.87 (br, 2H, >CH–), 1.42–1.15 (m, 96H, –$CH_2$–), 0.83–0.76 (m, 24H, –$CH_3$). $^{13}$C NMR (125 MHz, $CDCl_3$), $\delta$ (ppm): 163.52, 163.31, 163.13, 142.28, 140.19, 138.93, 135.04, 134.12, 133.30, 131.92, 131.57, 131.12, 129.46, 129.04, 128.70, 128.48, 127.70, 127.29, 126.67, 125.78, 124.15, 123.43, 44.75, 31.86, 31.81, 31.57, 30.00, 29.66, 29.55, 29.26, 22.63, 14.06. Elemental anal. calcd for $C_{112}H_{144}N_4O_8S$ (%): C, 78.83; H, 8.51; N, 3.28. Found (%), C, 78.76; H, 8.44; N, 3.39.

**Synthesis of 6-(*N*,*N*′-bis(2-hexyldecyl)perylenediimide-1-yl)-[1,12-*b*,*c*,*d*]selenophene-*N*,*N*′-bis(2-hexyldecyl)perylene diimide (PDI-SePDI).** The dimer **PDI-SePDI** was obtained by a similar method to that of **PDI-TPDI**, using **PDI-Bpin** (70.0 mg, 0.073 mmol) and **SePDIBr** (79.9 mg, 0.0803 mmol, 1.1 eq.). 32 mg **PDI-SePDI** was also obtained as a reddish-brown solid (yield = 23%). M.p. > 280 °C. $^1$H NMR (500 MHz, $CDCl_3$), $\delta$ (ppm): 9.52 (s, 1H, H of PDI), 9.44 (s, 1H, H of PDI), 8.89–8.83 (m, 2H, H of PDI), 8.77 (s, 2H, H of PDI), 8.67–8.59 (m, 2H, H of PDI), 8.50 (s, 1H, H of PDI), 8.43 (s, 1H, H of PDI), 8.19

 

(d, $^3J$ = 8.5 Hz, 1H, H of PDI), 7.88 (d, $^3J$ = 8.0 Hz, 1H, H of PDI), 4.13 (d, $^3J$ =7.0 Hz, 4H, >N–$CH_2$–), 4.06 (d, $^3J$ = 6.5 Hz, 2H, N–$CH_2$–), 4.01–3.98 (m, 2H, >N–$CH_2$–), 1.98 (br, 2H, >CH–), 1.89 (br, 2H, >CH–), 1.40–1.15 (m, 96H, –$CH_2$–), 0.85–0.77 (m, 24H, –$CH_3$). $^{13}$C NMR (125 MHz, $CDCl_3$), $\delta$ (ppm): 163.88, 163.48, 163.13, 141.81, 141.46, 140.76, 135.00, 134.39, 133.39, 132.82, 131.81, 131.54, 131.26, 130.35, 129.07, 128.95, 128.71, 126.82, 126.46, 124.18, 124.06, 123.58, 123.39, 123.18, 122.89, 122.73, 44.97, 44.76, 31.86, 31.81, 30.00, 29.66, 29.55, 29.26, 22.66, 22.63, 14.05. Elemental anal. calcd for $C_{112}H_{144}N_4O_8Se$ (%): C, 76.72; H, 8.28; N, 3.20. Found (%), C, 76.60; H, 8.20; N, 3.35.

## Author contributions

Junfeng Tong: conceptualization, investigation, writing – original draft. Jiayu Fang: writing & investigation. Lili An: investigation. Youzhi Huo: investigation. Fushui Di: investigation. Pengzhi Guo: calidation. Chunyan Yang: supervision. Zezhou Liang: supervision. Jianfeng Li: supervision. Yangjun Xia: review & editing.

## Data availability

The authors confirm that the data supporting the findings of this study are available within the article and its ESI.† Raw data that support the findings of this study are available from the corresponding author upon reasonable request.

## Conflicts of interest

There are no conflicts to declare.

## Acknowledgements

This work was financially supported by National Natural Science Foundation of China (62064006 and 52262026), Industrial support plan project of colleges and universities in Gansu Province (No.: 2021CYZC-19 and 2020C-07), West Light Foundation of the Chinese Academy of Sciences (No. 22JR9KA035), and the Natural Science Foundation of Gansu Province (23JRRA878).

## References

1 Y. Duan, X. Xu, H. Yan, W. Wu, Z. Li and Q. Peng, *Adv. Mater.*, 2017, **29**, 1605115.
2 G. Han and Y. Yi, *Acc. Chem. Res.*, 2022, **55**, 869–877.
3 Z. Luo, T. Liu, Z. Chen, Y. Xiao, G. Zhang, L. Huo, C. Zhong, X. Lu, H. Yan, Y. Sun and C. Yang, *Adv. Sci.*, 2019, **6**, 1802065.
4 L. Ye, W. Ye and S. Zhang, *J. Semicond.*, 2021, **42**, 101607.
5 X. Wang, Z. Li, X. Zheng, C. Xiao, T. Hu, Y. Liao and R. Yang, *Adv. Funct. Mater.*, 2023, **33**, 2300323.
6 L. Zhang, Z. Chen, F. Sun, Y. Wang, H. Bao, X. Gao and Z. Liu, *J. Electron. Mater.*, 2022, **51**, 4224–4237.
7 D. Zhou, J. Wang, Z. Xu, H. Xu, J. Quan, J. Deng, Y. Li, Y. Tong, B. Hu and L. Chen, *Nano Energy*, 2022, **103**, 107802.
8 Y. Cui, Y. Xu, H. Yao, P. Bi, L. Hong, J. Zhang, Y. Zu, T. Zhang, J. Qin, J. Ren, Z. Chen, C. He, X. Hao, Z. Wei and J. Hou, *Adv. Mater.*, 2021, **33**, 2102420.
9 Q. Liu, Y. Jiang, K. Jin, J. Qin, J. Xu, W. Li, J. Xiong, J. Liu, Z. Xiao, K. Sun, S. Yang, X. Zhang and L. Ding, *Sci. Bull.*, 2020, **65**, 272–275.
10 C. Li, J. Zhou, J. Song, H. Xu, J. Zhang, X. Zhang, J. Guo, L. Zhu, D. Wei, G. Han, J. Min, Y. Zhang, Z. Xie, Y. Yi, H. Yan, F. Gao, F. Liu and Y. Sun, *Nat. Energy*, 2021, **6**, 605–613.
11 J. Zhao, Y. Li, G. Yang, K. Jiang, H. Lin, H. Ade, W. Ma and H. Yan, *Nat. Energy*, 2016, **1**, 15027.
12 Y. Lin, J. Wang, Z.-G. Zhang, H. Bai, Y. Li, D. Zhu and X. Zhan, *Adv. Mater.*, 2015, **27**, 1170–1174.
13 W. Zhao, S. Li, H. Yao, S. Zhang, Y. Zhang, B. Yang and J. Hou, *J. Am. Chem. Soc.*, 2017, **139**, 7148–7151.
14 J. Yuan, Y. Zhang, L. Zhou, G. Zhang, H.-L. Yip, T.-K. Lau, X. Lu, C. Zhu, H. Peng, P. A. Johnson, M. Leclerc, Y. Cao, J. Ulanski, Y. Li and Y. Zou, *Joule*, 2019, **3**, 1140–1151.
15 J. Liu, S. Chen, D. Qian, B. Gautam, G. Yang, J. Zhao, J. Bergqvist, F. Zhang, W. Ma, H. Ade, O. Inganäs, K. Gundogdu, F. Gao and H. Yan, *Nat. Energy*, 2016, **1**, 16089.
16 D. Meng, D. Sun, C. Zhong, T. Liu, B. Fan, L. Huo, Y. Li, W. Jiang, H. Choi, T. Kim, J. Y. Kim, Y. Sun, Z. Wang and A. J. Heeger, *J. Am. Chem. Soc.*, 2016, **138**, 375–380.
17 G. Zhang, J. Feng, X. Xu, W. Ma, Y. Li and Q. Peng, *Adv. Funct. Mater.*, 2019, **9**, 1906587.
18 J. Zhang, Y. Li, J. Huang, H. Hu, G. Zhang, T. Ma, P. C. Y. Chow, H. Ade, D. Pan and H. Yan, *J. Am. Chem. Soc.*, 2017, **139**, 16092–16095.
19 K. Bhardwaj, S. Naqvi, S. K. Saini, M. Kumar and R. Kumar, *Sol. Energy*, 2022, **246**, 320–330.
20 P. Cheng, X. Zhao and X. Zhan, *Acc. Mater. Res.*, 2022, **3**, 309–318.
21 W. Liu, J. Fang, J. Tong, J. Qin, L. An, P. Guo, C. Yang, Z. Liang, J. Li and Y. Xia, *Dyes Pigm.*, 2024, **224**, 112038.
22 J. Tong, X. Jiang, Z. Dong, L. An, P. Guo, C. Yang, Z. Liang, J. Li and Y. Xia, *Dyes Pigm.*, 2022, **208**, 110816.
23 J. Tong, W. Liu, Y. Huang, Z. Li, Y. Wang, S. Bai, Z. Liang, L. Yan, J. Li and Y. Xia, *J. Mater. Chem. C*, 2023, **11**, 6951–6962.
24 M. Zhang, Y. Bai, C. Sun, L. Xue, H. Wang and Z.-G. Zhang, *Sci. China: Chem.*, 2022, **65**, 462–485.
25 R. Singh, E. Giussani, M. M. Mróz, F. D. Fonzo, D. Fazzi, J. Cabanillas-González, L. Oldridge, N. Vaenas, A. G. Kontos, P. Falaras, A. C. Grimsdale, J. Jacob, K. Müllen and P. E. Keivanidis, *Org. Electron.*, 2014, **15**, 1347–1361.
26 R. Singh, E. Aluicio-Sarduy, Z. Kan, T. Ye, R. C. I. MacKenzie and P. E. Keivanidis, *J. Mater. Chem. A*, 2014, **2**, 14348–14353.
27 J. Xiao, H.-J. Yu, D.-X. Xie, A. Shinohara, T. Fan, J. Yi, J. Y. L. Lai, G. Shao and H. Yan, *Sustainable Energy Fuels*, 2023, **7**, 294–299.

28 B. Carlotti, Z. Cai, H. Kim, V. Sharapov, I. K. Madu, D. Zhao, W. Chen, P. M. Zimmerman, L. Yu and T. Goodson, III, *Chem. Mater.*, 2018, **30**, 4263–4276.
29 P. Murugan, E. Ravindran, V. Sangeetha, S.-Y. Liu and J. W. Jung, *J. Mater. Chem. A*, 2023, **11**, 26393–26425.
30 S. Amiralaei, D. Uzun and H. Icil, *Photochem. Photobiol. Sci.*, 2008, **7**, 936–947.
31 K. Ding, T. Shan, J. Xu, M. Li, Y. Wang, Y. Zhang, Z. Xie, Z. Ma, F. Liu and H. Zhong, *Chem. Commun.*, 2020, **56**, 11433–11436.
32 K. C. Song, R. Singh, J. Lee, D. H. Sin, H. Lee and K. Cho, *J. Mater. Chem. C*, 2016, **4**, 10610–10615.
33 J. Lee, R. Singh, D. H. Sin, H. G. Kim, K. C. Song and K. Cho, *Adv. Mater.*, 2016, **28**, 69–76.
34 S. Chen, D. Meng, J. Huang, N. Liang, Y. Li, F. Liu, H. Yan and Z. Wang, *CCS Chem.*, 2021, **3**, 78–84.
35 W. Jiang, L. Ye, X. Li, C. Xiao, F. Tan, W. Zhao, J. Hou and Z. Wang, *Chem. Commun.*, 2014, **50**, 1024–1026.
36 Y. Zang, C.-Z. Li, C.-C. Chueh, S. T. Williams, W. Jiang, Z.-H. Wang, J.-S. Yu and A. K.-Y. Jen, *Adv. Mater.*, 2014, **26**, 5708–5714.
37 C.-H. Wu, C.-C. Chueh, Y.-Y. Xi, H.-L. Zhong, G.-P. Gao, Z.-H. Wang, L. D. Pozzo, T.-C. Wen and A. K.-Y. Jen, *Adv. Funct. Mater.*, 2015, **25**, 5326–5332.
38 H. Wang, L. Chen and Y. Xiao, *J. Mater. Chem. A*, 2017, **5**, 22288–22296.
39 D. Sun, D. Meng, Y. Cai, B. Fan, Y. Li, W. Jiang, L. Huo, Y. Sun and Z. Wang, *J. Am. Chem. Soc.*, 2015, **137**, 11156–11162.
40 J. Yang, F. Chen, P. Cong, H. Xiao, Y. Geng, Z. Liao, L. Chen, B. Zhang and E. Zhou, *J. Energy Chem.*, 2020, **40**, 112–119.
41 M. Li, H. Wang, Y. Liu, Y. Zhou, H. Lu, J. Song and Z. Bo, *Dyes Pigm.*, 2020, **175**, 108186.
42 H. Lu, H. Jin, H. Huang, W. Liu, Z. Tang, J. Zhang and Z. Bo, *Adv. Funct. Mater.*, 2021, **31**, 2103445.
43 C. Li, H. Fu, T. Xia and Y. Sun, *Adv. Energy Mater.*, 2019, **9**, 1900999.
44 F. Chen, G. Ding, A. Tang, B. Xiao, J. Li and E. Zhou, *J. Mater. Chem. C*, 2018, **6**, 2580–2587.
45 Y. Yin, J. Song, F. Guo, Y. Sun, L. Zhao and Y. Zhang, *ACS Appl. Energy Mater.*, 2018, **1**, 6577–6585.
46 L. Wang, H. Shen, X. You, D. Wu and J. Xia, *Eur. J. Org. Chem.*, 2022, e202101554.
47 G. Liu, T. Koch, Y. Li, N. L. Doltsinis and Z. Wang, *Angew. Chem.*, 2019, **131**, 184–189.
48 S. Kotha, K. Lahiri and D. Kashinath, *Tetrahedron*, 2002, **58**, 9633–9695.
49 J. Tong, X. Jiang, H. Li, L. An, C. Yang, Y. Huang, P. Guo, Z. Liang, C. Yang, J. Li and Y. Xia, *Opt. Mater.*, 2021, **121**, 111593.
50 M. Wang, X. Hu, P. Liu, W. Li, X. Gong, F. Huang and Y. Cao, *J. Am. Chem. Soc.*, 2011, **133**, 9638–9641.
51 J. Tong, J. Li, P. Zhang, X. Ma, M. Wang, L. An, J. Sun, P. Guo, C. Yang and Y. Xia, *Polymer*, 2017, **121**, 183–195.
52 Z. Chen, W. Zhang, J. Huang, D. Gao, C. Wei, Z. Lin, L. Wang and G. Yu, *Macromolecules*, 2017, **50**, 6098.
53 J. Tong, L. An, J. Li, J. Lv, P. Guo, L. Li, P. Zhang, C. Yang, Y. Xia and C. Wang, *J. Polym. Sci., Part A: Polym. Chem.*, 2018, **56**, 2059–2071.
54 J. Pommerehne, H. Vestweber, W. Guss, R. F. Mark, H. Bässles, M. Porsch and J. Daub, *Adv. Mater.*, 1995, **7**, 551–554.
55 Y. Li, *Acc. Chem. Res.*, 2012, **45**, 723–733.
56 M. J. Frisch, G. W. Trucks, H. B. Schlegel, G. E. Scuseria, M. A. Robb, J. R. Cheeseman, G. Scalmani, V. Barone, B. Mennucci, G. A. Petersson, H. Nakatsuji, M. Caricato, X. Li, H. P. Hratchian, A. F. Izmaylov, J. Bloino, G. Zheng, J. L. Sonnenberg, M. Hada, M. Ehara, K. Toyota, R. Fukuda, J. Hasegawa, M. Ishida, T. Nakajima, Y. Honda, O. Kitao, H. Nakai, T. Vreven, J. A. Montgomery, Jr., J. E. Peralta, F. Ogliaro, M. Bearpark, J. J. Heyd, E. Brothers, K. N. Kudin, V. N. Staroverov, R. Kobayashi, J. Normand, K. Raghavachari, A. Rendell, J. C. Burant, S. S. Iyengar, J. Tomasi, M. Cossi, N. Rega, J. M. Millam, M. Klene, J. E. Knox, J. B. Cross, V. Bakken, C. Adamo, J. Jaramillo, R. Gomperts, R. E. Stratmann, O. Yazyev, A. J. Austin, R. Cammi, C. Pomelli, J. W. Ochterski, R. L. Martin, K. Morokuma, V. G. Zakrzewski, G. A. Voth, P. Salvador, J. J. Dannenberg, S. Dapprich, A. D. Daniels, Ö. Farkas, J. B. Foresman, J. V. Ortiz, J. Cioslowski and D. J. Fox, Gaussian, Inc., Wallingford, CT, 2009.
57 H. Yao, D. Qian, H. Zhang, Y. Qin, B. Xu, Y. Cui, R. Yu, F. Gao and J. Hou, *Chin. J. Chem.*, 2018, **36**, 491–494.
58 Q. Xie, Y. Liu, X. Liao, Y. Cui, S. Huang, L. Hu, Q. He, L. Chen and Y. Chen, *Macromol. Rapid Commun.*, 2020, **41**, 2000454.
59 H. Yao, Y. Cui, D. Qian, Jr., C. S. Ponseca, A. Honarfar, Y. Xu, J. Xin, Z. Chen, L. Hong, B. Gao, R. Yu, Y. Zu, W. Ma, P. Chabera, T. Pullerits, A. Yartsev, F. Gao and J. Hou, *J. Am. Chem. Soc.*, 2019, **141**, 7743–7750.
60 T. Ye, R. Singh, H.-J. Butt, G. Floudas and P. E. Keivanidis, *ACS Appl. Mater. Interfaces*, 2013, **5**, 11844–11857.
61 C. Han, H. Gao, Y. Sun, Y. Kan, Z. Bi, W. Ma, Y. Zhang, J. A. Zapien, Y. Yang and K. Gao, *J. Energy Chem.*, 2024, **93**, 601–608.
62 Z. Liang, J. Tong, H. Li, Y. Wang, N. Wang, J. Li, C. Yang and Y. Xia, *J. Mater. Chem. A*, 2019, **7**, 15841–15850.
63 S. Rasool, Q. V. Hoang, D. V. Vu, C. E. Song, H. K. Lee, S. K. Lee, J.-C. Lee, S.-J. Moon and W. S. Shin, *J. Energy Chem.*, 2022, **64**, 236–245.
64 J. Li, Y. Wang, Z. Liang, N. Wang, J. Tong, C. Yang, X. Bao and Y. Xia, *ACS Appl. Mater. Interfaces*, 2019, **11**, 7022–7029.
65 C. Gu, Y. Zhao, X. Kang, X. Zhou, F. Bi, Y. Tian, Y. Li, J. Ma and X. Bao, *Polymer*, 2024, **299**, 126926.
66 L. Ye, Y. Xie, K. Weng, H. S. Ryu, C. Li, Y. Cai, H. Fu, D. Wei, H. Y. Woo, S. Tan and Y. Sun, *Nano Energy*, 2019, **58**, 220–226.
67 X. Liu, Z. Liang, S. Du, X. Niu, J. Tong, C. Yang, X. Lu, X. Bao, L. Yan, J. Li and Y. Xia, *ACS Appl. Mater. Interfaces*, 2022, **14**, 9386–9397.

 